Comput Geosci (2008) 12:525–539
DOI 10.1007/s10596-008-9092-z

ORIGINAL PAPER

# A space-time discontinuous Galerkin method applied to single-phase flow in porous media

**Zhiyun Chen · Holger Steeb · Stefan Diebels**

Received: 8 October 2007 / Accepted: 27 May 2008 / Published online: 29 August 2008
© Springer Science + Business Media B.V. 2008

**Abstract** A space-time discontinuous Galerkin finite element method is proposed and applied to a convection-dominant single-phase flow problem in porous media. The numerical scheme is based on a coupled space-time finite element discretization allowing for discontinuous approximations in space and in time. The continuities on the element interfaces are weakly enforced by the flux treatments, so that no extra penalty factor has to be determined. The resulting space-time formulation possesses the advantage of capturing the steep concentration front with sharp gradients efficiently. The stability and reliability of the proposed approach is demonstrated by numerical experiments.

**Keywords** Discontinuous Galerkin methods · Convection-dominant flow · Porous media

## 1 Introduction

The objective of this paper is to study an efficient numerical method for the simulation of miscible flow in porous media. The numerical investigation of such problems can be dated back to [1–3]. However, the traditional approaches, such as finite difference, finite volume, and continuous finite element methods, usually fail to capture the steep concentration fronts in heterogeneous porous materials. Since the last decade, more and more attention has been focused on the use of the discontinuous Galerkin (DG) methods in space to model convection-dominant flows in porous media [4–7]. The advantage of using such spatial DG approaches lies in the fact that these methods are locally mass-conservative and that they are able to capture the steep concentration front without extreme refinement in the discretization. Among the variety of different spatial DG formulations, there are some popular ones, such as the Oden–Baumann–Babuska (OBB) scheme [8], the nonsymmetric interior penalty Galerkin method (NIPG) [9], the symmetric interior penalty Galerkin method (SIPG) [10, 11], and the incomplete interior penalty Galerkin method (IIPG) [12, 13]. We mention that, except for the OBB formulation, the other three can be classified to the penalty method with a penalty factor $\sigma$. With a proper choice of this penalty factor, all four formulations lead to very similar numerical results [4, 14].

With respect to the dynamic modeling, it is common to solve the time-dependent problem, e.g., transport phenomena, in a semidiscrete manner, i.e., by means of the method of lines (MOL), such that the governing set of partial differential equations is first evaluated in space according to a finite element discretization to produce an ordinary differential equation system (ODE) in time, which can be, in turn, solved by a time difference approach, e.g., the Euler method, the Newmark method, etc. However, these time-stepping schemes are often known as having low efficiency, as

The author is grateful to the DFG (German Science Foundation—Deutsche Forschungsgemeinschaft) for the financial support under the grant number Di 430/4-2.

Z. Chen (✉) · H. Steeb · S. Diebels
Chair of Applied Mechanics, Saarland University,
Campus Saarbrücken, Building A 4.2,
66 123 Saarbrücken, Germany
e-mail: z.chen@mx.uni-saarland.de

S. Diebels
e-mail: s.diebels@mx.uni-saarland.de

they usually suffer from strong numerical dissipation and dispersion [15, 16]. Besides the time difference approaches, studies of using finite element method in time can be dated back to 1960s [17–19]. Using finite element discontinuous approximation in time was first proposed by Hughes and Hulbert [20]. Therein, they proposed a decoupled space-time Galerkin method, in which a continuous Galerkin approximation is applied in space to produce an ODE system, which is then evaluated by a DG approach in time, cf. [21–23]. This method is also known as a semidiscrete approach in that the spatial and temporal integrations are evaluated subsequently. In the previous work of the authors, we investigated a space-time coupled DG formulation. By use of finite element shape function consisting of tensor products of polynomials in space and in time, we are able to evaluate the spatial and temporal integration simultaneously. As the finite element approximation is continuous in space but discontinuous in time, the method is called the time-discontinuous Galerkin method (DGT) [24]. In contrast to decoupled methods, i.e., semidiscrete methods, a coupled formulation has an advantage in less numerical dispersion and dissipation. Moreover, it is easy to develop a simple efficient space-time discretization scheme based on the coupled formulation. Higher-order methods can be achieved straightforwardly by employing higher-order polynomials in space and in time.

In the current work, we combined the DG approach in time with the OBB formulation [25] in space to construct a coupled numerical formulation that is continuous in neither space nor time. We remark that, as the treatments of enforcing the continuity in time and in space are decoupled, such a combination of the DG approaches in space and in time generally allowed. In addition, other popular spatial DG formulations, i.e., NIPG, SIPG, and IIPG, combined with the DG approach in time have also been tested. It has to be mentioned that, with a proper choice of the penalty factor, no significant difference has been observed in the numerical solutions.

The structure of the current work is as follows: in the next section, we discuss briefly about the modeling aspect of the miscible flow through porous materials. After that, a coupled space-time discontinuous Galerkin (DGST) formulation for the solution of model equations is proposed. In the next section, some numerical experiments are performed in order to demonstrate the behavior of the new space-time coupled scheme. We close our discussion with a short conclusion.

## 2 Physical modeling

The physical model describes the procedure of a liquid mixture through a rigid porous skeleton with a constant porosity $\phi(\mathbf{x}, t)$. The liquid mixture $\varphi^{\mathfrak{l}}$ consists of a resident fluid $\varphi^{\mathfrak{f}}$ and a solvent fluid $\varphi^{\mathfrak{a}}$, i.e., $\varphi^{\mathfrak{l}} = \varphi^{\mathfrak{f}} \cup \varphi^{\mathfrak{a}}$. The partial density of the liquid mixture $\rho$ is given by $\rho = \rho^{\mathfrak{a}} + \rho^{\mathfrak{f}}$, in which $\rho^{\mathfrak{a}}$ and $\rho^{\mathfrak{f}}$ represent the partial density of the solvent and the resident fluid, respectively. The *mass-specific* concentration $c$ of the solvent fluid is defined as $c := \rho^{\mathfrak{a}}/\rho$. For the sake of simplicity, we assume that the density $\rho$ of the liquid mixture is a constant. Next, we introduce the *barotropic velocity* of the liquid mixture as $\mathbf{v} = (\rho^{\mathfrak{f}}\mathbf{v}_{\mathfrak{f}} + \rho^{\mathfrak{a}}\mathbf{v}_{\mathfrak{a}})/\rho$, in which $\mathbf{v}_{\mathfrak{f}}$ and $\mathbf{v}_{\mathfrak{a}}$ represent the velocity of the resident and the solvent fluid, respectively. Note that this *barotropic velocity* can be further related to the *filter velocity* or Darcy's velocity $\mathbf{q}$ through $\mathbf{q} := \phi\,\mathbf{v}$. The *diffusion velocity* $\mathbf{d}_{\mathfrak{a}}$ is introduced as $\mathbf{d}_{\mathfrak{a}} = \mathbf{v}_{\mathfrak{a}} - \mathbf{v}$.

Taking into consideration that the porous skeleton is rigid, the field equations of the system can be obtained by evaluating the continuity equation, the momentum balance of the liquid mixture $\varphi^{\mathfrak{l}}$, and the mass balance of the solvent fluid $\varphi^{\mathfrak{a}}$ as

$$\operatorname{div}\mathbf{v} = 0, \tag{1}$$

$$\rho\,\mathbf{a}_{\mathfrak{l}} - \operatorname{div}\mathbf{T}^{\mathfrak{l}} = \hat{\mathbf{p}}^{\mathfrak{l}} + \rho\,\mathbf{b}, \tag{2}$$

$$\phi\,\rho\,\partial_t(c) + \operatorname{div}(\mathbf{j}_{\mathfrak{a}} + \phi\,c\,\rho\,\mathbf{v}) = 0. \tag{3}$$

In Eq. 2, $\mathbf{T}^{\mathfrak{l}}$ denotes the Cauchy stress tensor, $\rho\mathbf{b}$ is the volume force, and $\mathbf{a}_{\mathfrak{l}}$ stands for the acceleration of the liquid mixture. $\hat{\mathbf{p}}^{\mathfrak{l}}$ represents the momentum exchange between the liquid mixture $\varphi^{\mathfrak{l}}$ and solid phase $\varphi^{\mathfrak{s}}$. The stress tensor of the liquid mixture can be further written as $\mathbf{T}^{\mathfrak{l}} = -\phi\,p\,\mathbf{I} + \mathbf{T}^{\mathfrak{l}}_{\mathrm{E}}$, with $p$ denoting the fluid pressure and $\mathbf{T}^{\mathfrak{l}}_{\mathrm{E}}$ denoting the so-called extra stress of the liquid mixture. An order-of-magnitude analysis [26, 27] shows that, for standard conditions of liquid flow in porous media, the extra stress $\mathbf{T}^{\mathfrak{l}}_{\mathrm{E}}$ of the liquid mixture is of higher order, which is not counted here. The momentum exchange $\hat{\mathbf{p}}^{\mathfrak{l}}$ can be expressed as the sum of an equilibrium part $\hat{\mathbf{p}}^{\mathfrak{l}}_{\mathrm{eq}}$ and a nonequilibrium part $\hat{\mathbf{p}}^{\mathfrak{l}}_{\mathrm{neq}}$, i.e., $\hat{\mathbf{p}}^{\mathfrak{l}} = \hat{\mathbf{p}}^{\mathfrak{l}}_{\mathrm{eq}} + \hat{\mathbf{p}}^{\mathfrak{l}}_{\mathrm{neq}}$, cf. [28]. Usually, the equilibrium part $\hat{\mathbf{p}}_{\mathrm{eq}}$ is proportional to the gradient of the porosity $\phi$ and the pore pressure $p$, i.e., $\hat{\mathbf{p}}^{\mathfrak{l}}_{\mathrm{eq}} = p\,\operatorname{grad}\phi$, while the nonequilibrium part $\hat{\mathbf{p}}_{\mathrm{neq}}$ is an isotropic vector-valued function of the nonequilibrium process variable $\mathbf{v}$. In the simplest case, it is a linear function of $\mathbf{v}$, i.e., $\hat{\mathbf{p}}^{\mathfrak{l}}_{\mathrm{neq}} = -[(\phi^2\,\mu^{\mathfrak{l}})/k^{\mathfrak{s}}]\,\mathbf{v}$, in which $\mu^{\mathfrak{l}}$ and $k^{\mathfrak{s}}$ are the dynamic

viscosity of the liquid mixture and the so-called intrinsic permeability of the solid skeleton, respectively. Generally, the dynamic viscosity of the liquid mixture $\mu^{\mathfrak{l}}$ is a function of the concentration $c$, i.e., $\mu = \mu^{\mathfrak{l}}(c)$. Moreover, since the liquid acceleration $\mathbf{a}_{\mathfrak{l}}$ is mostly very small, it is common to neglect this term, i.e., $\mathbf{a}_{\mathfrak{l}} = \mathbf{0}$ in Eq. 2. Thus, Eq. 2 boils down to Darcy's equation

$$\mathbf{q} = \frac{k^{\mathfrak{s}}}{\mu^{\mathfrak{l}}} \operatorname{grad} p. \tag{4}$$

In Eq. 3, the diffusion flux $\mathbf{j}_{\mathfrak{a}}$ can be modeled by Fick's law given by $\mathbf{j}_{\mathfrak{a}} = -\mathbf{D} \cdot \operatorname{grad} \rho^{\mathfrak{a}}$, in which $\mathbf{D}$ denotes the second-order diffusion tensor. Note that, in the current work, we do not consider mass exchanges, e.g., chemical reactions between the solvent and the resident fluid. Inserting Fick's law Eq. 3, and Eq. 4 into the continuity equation Eq. 1, we obtain the set of field equations on the spatial domain $\Omega \in \mathbb{R}^2$ over the time $\mathcal{I} = [t_0,\ T]$ as

$$\phi\, \partial_t(c) + \operatorname{div}(c\,\mathbf{q} - \mathbf{D} \operatorname{grad} c) = 0, \quad \text{in} \quad \Omega \times \mathcal{I}, \tag{5}$$

$$\operatorname{div}\left[\frac{k^{\mathfrak{s}}}{\mu^{\mathfrak{l}}} \operatorname{grad} p\right] = 0 \equiv \operatorname{div} \mathbf{q}, \quad \text{in} \quad \Omega \times \mathcal{I}. \tag{6}$$

The boundary $\partial\Omega$ consists of nonoverlapping Dirichlet part $\Gamma_{\mathrm{D}}^{\mathfrak{a}/\mathfrak{l}}$ and the Neumann part $\Gamma_{\mathrm{N}}^{\mathfrak{a}/\mathfrak{l}}$ of the liquid mixture $\varphi^{\mathfrak{l}}$ and the solvent fluid $\varphi^{\mathfrak{a}}$, respectively, i.e., $\partial\Omega = \Gamma_{\mathrm{D}}^{\mathfrak{l}/\mathfrak{a}} \cup \Gamma_{\mathrm{N}}^{\mathfrak{l}/\mathfrak{a}}$ and $\Gamma_{\mathrm{D}}^{\mathfrak{l}/\mathfrak{a}} \cap \Gamma_{\mathrm{N}}^{\mathfrak{l}/\mathfrak{a}} = \emptyset$. The boundary conditions are given for the pressure $p$ and for the concentration $c$ as

$$\begin{aligned} p &= \bar{p} \quad \text{on} \quad \Gamma_{\mathrm{D}}^{\mathfrak{l}} \times \mathcal{I}, \\ c &= \bar{c} \quad \text{on} \quad \Gamma_{\mathrm{D}}^{\mathfrak{a}} \times \mathcal{I}, \\ \mathbf{q} \cdot \mathbf{n} &= \bar{q} \quad \text{on} \quad \Gamma_{\mathrm{N}}^{\mathfrak{l}} \times \mathcal{I}, \\ (c\,\mathbf{q} - \mathbf{D} \cdot \operatorname{grad} c) \cdot \mathbf{n} &= c_{\mathrm{in}} \quad \text{on} \quad \Gamma_{\mathrm{N}}^{\mathfrak{a}} \times \mathcal{I}, \end{aligned} \tag{7}$$

in which $\bar{p}$ and $\bar{c}$ are the pressure and concentration prescribed on the Dirichlet boundaries. The inflow flux of the liquid mixture is denoted by $\bar{q}$ and the concentration of the inflow fluid is $c_{\mathrm{in}}$. $\mathbf{n}$ stands for the unit outward normal vector on the boundary.

The associated initial conditions at $t = t_0$ are given for the fluid pressure $p$ and the concentration $c$ as

$$p = p_0 \quad \text{at} \quad \Omega \times t_0, \qquad \text{and} \qquad c = c_0 \quad \text{at} \quad \Omega \times t_0. \tag{8}$$

## 3 Finite element weak form

In the current work, we investigate a coupled DGST method for the solution strategy of single-phase flow problems. The space-time domain $Q$ is constructed by adding the time axis orthogonal to the spatial domain $\Omega$, i.e., $Q = \Omega \times \mathcal{I}$. The temporal domain $\mathcal{I}$ is discretized into a sequence of time intervals $\mathcal{I}^n = [t_n, t_{n+1})$, with $t_n < t_{n+1}$. As a consequence, we introduce the discrete space-time slab as $Q^n = \Omega \times \mathcal{I}^n$, rf. [24]. Let $\mathcal{E}_h = \{E_1, E_2, \ldots, E_{N_E}\}$ be subdivisions of the discrete spatial domain $\Omega_h \in \Omega$ consisting of triangles or quadrilaterals. The edges of each subdivision $E_i$ are denoted by $\partial E_i$ $(i < N_E)$. The union of all edges in $\mathcal{E}_h$ is denoted by $\mathcal{K}_h = \{e_1, e_2, \ldots, e_{N_K}\}$. The interior edges shared by two adjacent subdivisions are denoted as $\Gamma_{\mathrm{int}} = \{\partial E_i \cap \partial E_j, i \neq j\}$. Furthermore, we denote the unit outward normal vector on $\partial E_i$ that coincides with the edge $e_k$ by $\mathbf{n}_i^k$ and $\mathbf{n}_i$ stands for the union of all outward normal vectors on $\partial E_i$. Figure 1 shows examplarily one of such a finite element patches with four quadrilaterals.

Moreover, according to the direction of the flows over the edges, we can divide the edge $\mathcal{K}_h$ into an inflow part $\mathcal{K}_h^-$ and an outflow part $\mathcal{K}_h^+$,

$$\begin{aligned} \mathcal{K}_h^- &= \{\mathbf{x} \in (e_k \cap \partial E_i) : \left(\tilde{\mathbf{q}}_h(\mathbf{x}) \cdot \mathbf{n}_i^k(\mathbf{x})\right) > 0\}, \\ \mathcal{K}_h^+ &= \mathcal{K}_h \setminus \mathcal{K}_h^-. \end{aligned} \tag{9}$$

Analogically, each interior edge $e_k \in \Gamma_{\mathrm{int}}$ can be further divided into an inflow and an outflow part, i.e., $e_k = e_k^- \cup e_k^+$ with $e_k^- \in \mathcal{K}_h^-$ and $e_k^+ \in \mathcal{K}_h^+$.

Note that, due to a discontinuous approximation of the pressure $p_h$, different values of the filter velocities $\mathbf{q}_h^{\mathrm{DG}} = (k^{\mathfrak{s}}/\mu^{\mathfrak{l}}) \operatorname{grad} p_h$ are evaluated from both sides of the interior edge. In Eq. 9, $\tilde{\mathbf{q}}_h$ stands for the continuous projection of the filter velocity $\mathbf{q}_h^{\mathrm{DG}}$ on edges. More details concerning the projection approach will be mentioned later.

Next, we denote the normal vector as $\mathbf{n}_j^k = \sum_d (n_d\, \mathbf{e}_d)$, $(d = 1, 2)$, in which $\mathbf{e}_d$ are the basis vectors. The operator $\{\mathbf{n}_j^k\}$ is defined as $\{\mathbf{n}_j^k\} = \sum_d (n_d\, \mathbf{e}_d \cdot \mathbf{e}_d)$, $(d = 1, 2)$. The vector $\mathbf{n}_i^k$ is considered as positive if $\{\mathbf{n}_i^k\} > 0$. According to the direction of the positive normal vector, we can uniquely define the jump on this edge. Assume that $e_k$ is the interior edge shared by the two finite elements $E_i$ and $E_j$, i.e., $e_k = \partial E_i \cap \partial E_j$. For $\{\mathbf{n}_i^k\} > 0$, we define the jump of a function $\psi$ as

$$[\![\, \psi(\mathbf{x}, t) \,]\!]_{e_k} = \psi_j(\mathbf{x}, t) - \psi_i(\mathbf{x}, t), \ \ \mathbf{x} \in e_k, \ \ \{\mathbf{n}_i^k\} > 0, \tag{10}$$

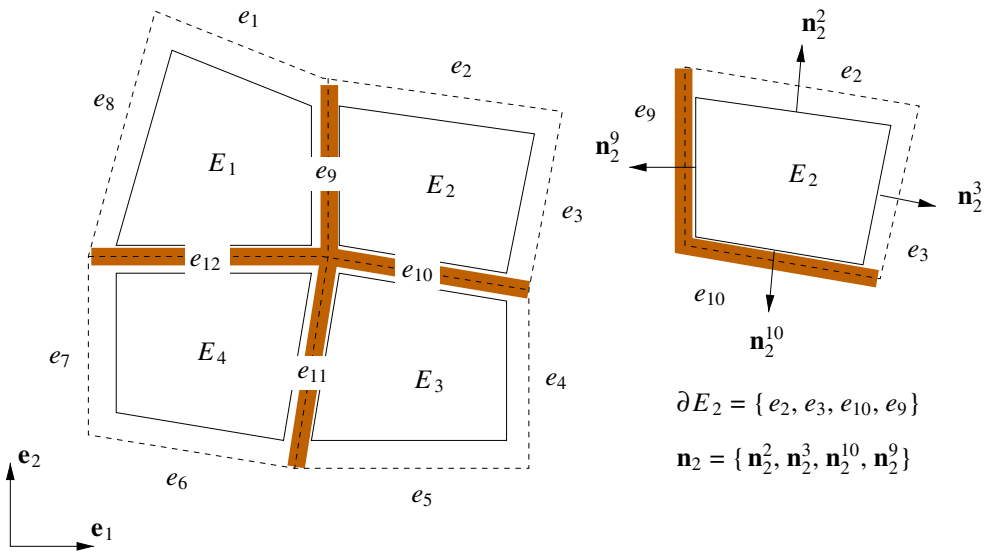


**Fig. 1** A finite element patch of four quadrilaterals $\mathcal{E}_h = \{E_1 \sim E_4\}$ with the boundaries $\mathcal{K}_h = \{e_1 \sim e_{12}\}$, among which $\{e_9 \sim e_{12}\}$ are interior edges

where $\psi_l = \{\psi(\mathbf{x}, t) : \mathbf{x} \in (e_k \cap \partial E_l)\}$, $(l = i, j)$. The jumps may be defined for the concentration and the pressure, i.e., $\psi \in \{c, p\}$. Furthermore, the average of a vector $\Psi$ on the edge $e_k$ is defined as

$$\langle \Psi(\mathbf{x}, t) \cdot \mathbf{n} \rangle|_{e_k} = \frac{1}{2}\left(\Psi_i(\mathbf{x}, t) \cdot \mathbf{n}_i^k + \Psi_j(\mathbf{x}, t) \cdot \mathbf{n}_i^k\right), \quad \{\mathbf{n}_i^k\} > 0, \tag{11}$$

with $\Psi_l(\mathbf{x}, t) = \{\Psi(\mathbf{x}, t) : \mathbf{x} \in (e_k \cap \partial E_l)\}$, $(l = i, j)$. This operation is required for the flux terms, i.e., $\Psi = \{(\mathbf{D} \cdot \operatorname{grad} c), (k^{\mathfrak{s}}/\mu^{\mathfrak{l}}) \operatorname{grad} p\}$. In addition, according to the direction of the flow, we define the spatial *upwind* flux $\psi^{\text{in}}$ on the edge $e_k$ as

$$\psi^{\text{in}}(\mathbf{x}, t)|_{e_k} = \begin{cases} \psi_i(\mathbf{x}, t), & \text{if} \quad (\tilde{\mathbf{q}} \cdot \mathbf{n}_i^k) > 0, \\ \psi_j(\mathbf{x}, t), & \text{otherwise.} \end{cases} \tag{12}$$

According to the above definition, the flux $\psi^{\text{in}}$ on the interior edge $e_k$ equals the value on its inflow part $e_k^-$. In Fig. 2a, we depict examplarily the spatial *upwind* flux $\psi^{\text{in}}$ on a finite element patch of four quadrilaterals. We remark that, due to the introduction of the flux treatment on the boundaries, the Dirichlet boundary conditions are assigned as inflow flux rather than strict assignments, i.e., $\Gamma_D^{\mathfrak{l}/\mathfrak{a}} \in \mathcal{K}_h^-$, cf. [29].

Analog to the spatial *upwind* flux definition, we define the temporal *upwind* flux $\breve{\psi}_n$ at time $t_n$ as, cf. [24, 30]

$$\breve{\psi}_n(\mathbf{x}) = \begin{cases} \psi_0(\mathbf{x}), & \text{if} \quad n = 0 \\ \psi^-(\mathbf{x}, t_n), & \text{otherwise,} \end{cases} \tag{13}$$

with

$$\psi^-(\mathbf{x}, t_n) = \lim_{\varepsilon \to 0^+} \psi(\mathbf{x}, t_n - \varepsilon), \tag{14}$$

where $\varepsilon$ is an infinitely small positive number. The temporal *upwind* definition $\breve{\psi}_n$ implies that the value of $\psi$ at the discrete time level $t_n$ equals its immediate previous value $\psi^-(t_n)$. For $n > 0$, the immediate previous value $\psi^-(t_n)$ results from the previous computation on the time-slab $Q^{n-1}$ at time $t_n$, while for the initial step $n = 0$, $\breve{\psi}_0$ stands for the initial condition, see Fig. 2b. Obviously, such a definition fulfills the causality condition that the information travels "*from the past to the future*". Moreover, we denote that the algebraic solution schemes on each time-slab are decoupled, so that $\breve{\psi}_n$ serves as the initial condition for the current time-slab $Q^n$. Such a sequential solution scheme is favorable as it avoids a huge algebraic system consisting of the total number of degrees of freedom (DOFs) on the space-time domain $Q$. Nevertheless, adopting larger time step sizes without degenerating numerical accuracy can be easily achieved by employing higher-order polynomials in time. A further discussion of the temporal *upwind* flux technique can be found in [24, 30].

Let $\mathcal{W}$ be the finite dimensional functional space consisting of tensor products in space and in time. $\mathcal{W}$ consists of discontinuous piecewise polynomials over the subdomains $E_j$ and the time intervals $\mathcal{I}^n$. Figure 3 examplarily shows a one-dimensional spatial problem with four finite elements in space and three time-slabs in the temporal domain. Herein, linear polynomials in space and in time are employed. Noting that, since the flux treatments in space and in time are decoupled, we construct the finite element weak form by combining the spatial DG scheme with the DG scheme in time [24] directly. In the current work, we construct the spatial discretization of Eq. 6 with the OBB scheme [31], while Eq. 5 is formulated by the OBB scheme,

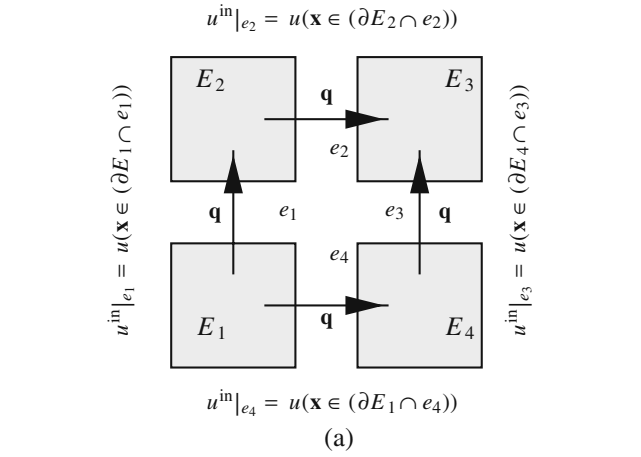


**Fig. 2** *Upwind* fluxes in space and in time. (**a**) *Upwind* flux $\psi^{\text{in}}|_{e_i}$ in space. (**b**) *Upwind* flux $\breve{\psi}(t_n)$ in time

the NIPG scheme [9], the SIPG scheme [10, 11], or the IIPG scheme [12, 13]. We note that these four spatial formulations are very similar, which can be identified by a pair of parameters $\epsilon$ and $\sigma$ (cf. [4]). The resulting space-time finite element problem can be formulated as follows:

*Find* $\mathbf{u}_h = [c_h, p_h]^T \in \mathcal{W}$, *such that* $\forall \delta\mathbf{u}_h = [\delta c_h, \delta p_h]^T \in \mathcal{W}$ *there exists*

$$B(\mathbf{u}_h, \delta\mathbf{u}_h) = L(\delta\mathbf{u}_h). \tag{15}$$

The discrete bilinear form $B(\mathbf{u}_h, \delta\,\mathbf{u}_h)$ and the linear form $L(\delta\mathbf{u}_h)$ are

$$\begin{aligned} &B(\mathbf{u}_h, \delta\mathbf{u}_h) \\ &= \sum_{j=1}^{N_E} \Bigg\{ \int_{E_j \times \mathcal{I}^n} \Big\{ -\phi\, c_h\, \partial_t(\delta c_h) + \frac{k^{\mathfrak{s}}}{\mu^{\mathfrak{l}}} \operatorname{grad} p_h \cdot \operatorname{grad} \delta p_h \\ &\qquad + (\mathbf{D} \operatorname{grad} c_h) \cdot \operatorname{grad} \delta c_h \\ &\qquad - c_h (\mathbf{q}_h \cdot \operatorname{grad} \delta c_h) \Big\} \,\mathrm{d}v\,\mathrm{d}t \\ &\qquad + \int_{(\partial E_j \setminus \Gamma_D^{\mathfrak{a}}) \times \mathcal{I}^n} (\tilde{\mathbf{q}}_h \cdot \mathbf{n}_j)\, c_h^{\text{in}}\, \delta c_h \,\mathrm{d}a\,\mathrm{d}t \\ &\qquad + \int_{E_j} \phi\, c_{h,n+1}^{-}\, \delta c_h \,\mathrm{d}v \Bigg\} \\ &+ \sum_{k=1}^{P_e} \Bigg\{ \int_{e_k \times \mathcal{I}^n} \Big\{ \Big\langle \frac{k^{\mathfrak{s}}}{\mu^{\mathfrak{l}}} \operatorname{grad} \delta p_h \cdot \mathbf{n} \Big\rangle [\![\, p_h \,]\!] \\ &\qquad - \Big\langle \frac{k^{\mathfrak{s}}}{\mu^{\mathfrak{l}}} \operatorname{grad} p_h \cdot \mathbf{n} \Big\rangle [\![\, \delta p_h \,]\!] \end{aligned}$$

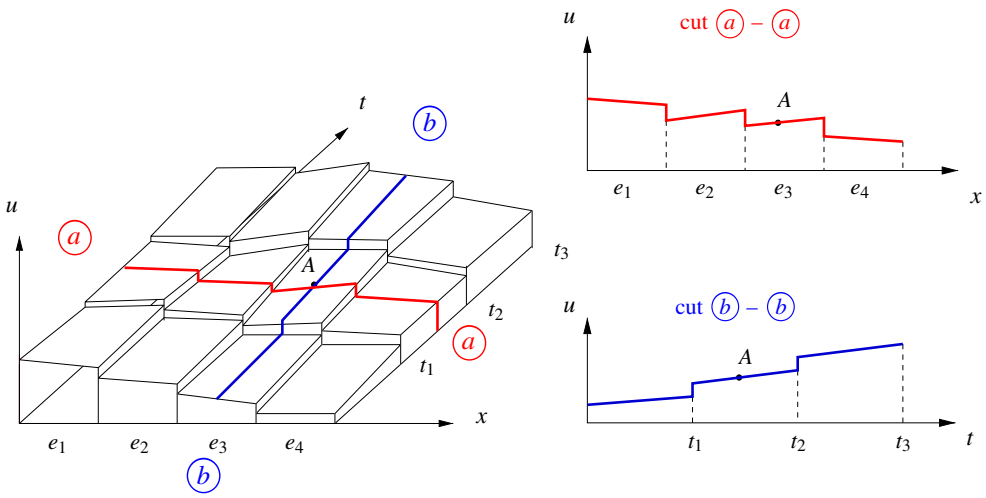


**Fig. 3** Finite element approximation of a 1-dim spatial problem with both linear polynomials in space and in time of the DGST formulation

$$
\begin{aligned}
&+\epsilon\,\langle(\mathbf{D}\ \mathrm{grad}\,\delta c_h)\cdot\mathbf{n}\rangle[\![\,c_h\,]\!]\\
&-\langle(\mathbf{D}\ \mathrm{grad}\,c_h)\cdot\mathbf{n}\rangle[\![\,\delta c_h\,]\!]\\
&+\sigma\,[\![\,c_h]\!]\,[\![\delta c_h]\!]\Big\}\,\mathrm{d}a\,\mathrm{d}t\Big\}\\
&+\sum_{e_k\in\Gamma_D^{\mathfrak{l}}}\Bigg\{\int_{e_k\times\mathcal{I}^n}\Big\{\Big(\frac{k^{\mathfrak{s}}}{\mu^{\mathfrak{l}}}\,\mathrm{grad}\,\delta p_h\cdot\mathbf{n}\Big)\,p_h\\
&\qquad-\Big(\frac{k^{\mathfrak{s}}}{\mu^{\mathfrak{l}}}\,\mathrm{grad}\,p_h\cdot\mathbf{n}\Big)\,\delta p_h\Big\}\,\mathrm{d}a\,\mathrm{d}t\Bigg\}\\
&+\sum_{e_k\in\Gamma_D^{\mathfrak{a}}}\Bigg\{\int_{e_k\times\mathcal{I}^n}\Big\{\epsilon\,\Big((\mathbf{D}\,\mathrm{grad}\,\delta c_h)\cdot\mathbf{n}\Big)\,c_h\\
&\qquad-\Big((\mathbf{D}\,\mathrm{grad}\,c_h)\cdot\mathbf{n}\Big)\,\delta c_h+\sigma\,c_h\,\delta c_h\Big\}\,\mathrm{d}a\,\mathrm{d}t\Bigg\},
\end{aligned}
\tag{16}
$$

$$
\begin{aligned}
L(\delta\mathbf{u}_h)=&\sum_{e_k\in\Gamma_D^{\mathfrak{l}}}\Bigg\{\int_{e_k\times\mathcal{I}^n}\Big\{\Big(\frac{k^{\mathfrak{s}}}{\mu^{\mathfrak{l}}}\,\mathrm{grad}\,\delta p_h\cdot\mathbf{n}\Big)\,\bar{p}\Big\}\,\mathrm{d}a\,\mathrm{d}t\Bigg\}\\
&+\sum_{e_k\in\Gamma_N^{\mathfrak{l}}}\Bigg\{\int_{e_k\times\mathcal{I}^n}\bar{q}\,\delta p\,\mathrm{d}a\,\mathrm{d}t\Bigg\}\\
&+\sum_{e_k\in\Gamma_D^{\mathfrak{a}}}\Bigg\{\int_{e_k\times\mathcal{I}^n}\Big\{\epsilon\,\Big((\mathbf{D}\,\mathrm{grad}\,\delta c_h)\cdot\mathbf{n}\Big)\,\bar{c}\\
&\qquad-(\tilde{\mathbf{q}}_h\cdot\mathbf{n})\,\bar{c}\,\delta c_h+\sigma\,\bar{c}\,\delta c_h\Big\}\mathrm{d}a\,\mathrm{d}t\Bigg\}\\
&+\sum_{e_k\in\Gamma_N^{\mathfrak{a}}}\Bigg\{\int_{e_k\times\mathcal{I}^n}c_{\mathrm{in}}\,\delta c_h\,\mathrm{d}a\,\mathrm{d}t\Bigg\}\\
&+\sum_{j=1}^{N_E}\Bigg\{\int_{E_j}\phi\,\check{c}_{h,n}\,\delta c_h\,\mathrm{d}v\Bigg\}.
\end{aligned}
\tag{17}
$$

Herein, $P_e$ denotes the total number of interior edges. In Eq. 16, the filter velocity $\mathbf{q}_h$ equals $(k^{\mathfrak{s}}/\mu^{\mathfrak{l}})\ \mathrm{grad}\ p_h$, which introduce the nonlinear coupling into the governing set of equations. In the current work, the nonlinear set of equations is linearized and solved by a global Newton–Raphson scheme [32, 33]. The integral $\int_{E_j}(\cdot)\,\mathrm{d}v$ has to be evaluated at the borders of the time-slab $t_n$ and $t_{n+1}$. Since the quantity of the *upwind* flux $\check{c}_{h,n}$ is always known on the current time-slab $Q^n$, the integral $\{\int_{E_j}\phi\,\check{c}_{h,n}\,\delta c_h\,\mathrm{d}v\}$ can be evaluated explicitly in the linear form $L(\delta\mathbf{u}_h)$. The parameters $\epsilon$ and $\sigma$ designate the various spatial schemes for Eq. 5, in particular, OBB, $\epsilon=1$ and $\sigma=0$; SIPG, $\epsilon=-1$ and $\sigma>0$; NIPG, $\epsilon=1$ and $\sigma>0$; and IIPG, $\epsilon=0$ and $\sigma>0$. It can be observed that, in the above expressions, the parameter $\sigma$ is a purely penalty factor that controls the quantities of jumps, i.e., $[\![c_h]\!]$, on edges. It has also to be mentioned, according to a proper choice of the penalty factor $\sigma$, that these four approaches lead to very similar numerical solutions. In the latter context, without special notification, the system of Eqs. 5 and 6) is solved by the OBB–OBB formulation, i.e. $\epsilon=1$, $\sigma=0$.

Recall that $\tilde{\mathbf{q}}_h$ represents the continuous projection of the discontinuous filter velocity $\mathbf{q}_h^{\mathrm{DG}}$ on the edges. As we now apply discontinuous approximations in space, different quantities of the filter velocity $\mathbf{q}_h^{\mathrm{DG}}=(k^{\mathfrak{s}}/\mu^{\mathfrak{l}})\,\mathrm{grad}\,p_h$ are evaluated from the adjacent elements on both sides of the interior edge. Such an inconsistency raises spurious oscillations that may further spoil the overall solution [14, 34]. Thus, a conservative projection resulting in continuous normal components of the filter velocities $\tilde{\mathbf{q}}_h$ over the element boundaries is necessary. In the present work, for the sake of simplicity, we apply the $H(\mathrm{div})$ projection [34] for the computation of $\tilde{\mathbf{q}}_h$ in a postprocessing step. Therefore, for the computation of the current time-slab $Q^n$ $(n>0)$, $\tilde{\mathbf{q}}$ is a result of the projected velocity at $t_n^-$. As for the initial step, i.e., $Q^0$, as there is no previous computation available, we assume that $\tilde{\mathbf{q}}_h=\mathbf{q}_h$ and solve the nonlinear set of equations by a global Newton–Raphson scheme [32, 33].

It is well known that, in the DG formulation for linear or higher-order polynomials in space, it is usually necessary to apply a slope-limiting procedure to avoid over- and undershoot in the neighborhood of concentration fronts, cf. [4, 35]. In the present work, by using the DGT formulation in time, $\check{c}_{h,n}$ serves as the only input information for the computation of the current time-slab $Q^n$. Note that this is either a result $c_{h,n}^-$ obtained from the previous time-slab $Q^{n-1}$ $(n>1)$ or the initial condition $c_0$ given at $t=t_0$. Here, we apply the slope-limiting procedure to $c_{h,n}^-$ $(n>0)$ in a postprocessing step. Therefore, only regular quantities of $\check{c}_{h,n}$ occur in the input data for the computation on the current time-slab $Q^n$. We note that, with respect to the numerical experiments performed in our work, it is sufficient to apply the slope-limiting procedure to the concentration $c_h$ to ensure the stability of the solution.

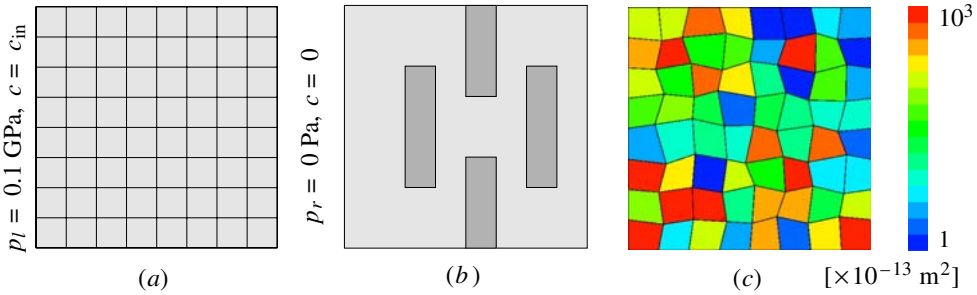


**Fig. 4** Boundary conditions and permeability distributions (*a–c*)

A stabilization procedure to the pressure $p_h$ is not involved. Note that this is different from the most semi-discrete approaches employing time difference schemes for simulating dynamic phenomena, which depends on the chosen finite difference procedure in time, a consistent slope limiting procedure for the primary unknown and its rate term must be developed, see, e.g., [35]. In the current work, we apply the quadratic slope limiter [36] for the limiting procedure of the concentration $c^-_{h,n}$.

## 4 Numerical experiments

In the following numerical experiments, we consider a square domain of the geophysical size $1{,}600 \times 1{,}600\,\text{m}^2$, which is subjected to a pressure difference on the left side of $p_l = 0.1$ GPa and on the right side of $p_r = 0$. A solvent fluid with the concentration $c_{\text{in}} = 1$ is injected from the left side into the domain, see Fig. 4a. Here, we apply quadratic spatial polynomials and linear temporal ones for the approximations of the pressure $p_h$ and the concentration $c_h$.

According to [37], for the two-dimensional case, the diffusion tensor $\mathbf{D}(\mathbf{q})$ depending on the filter velocities $\mathbf{q} = [q_1, q_2]^T$ is given by

$$\mathbf{D}(\mathbf{q}) = \phi\, d_m\, \mathbf{I} + \frac{\alpha_l}{|\mathbf{q}|}\begin{pmatrix} q_1^2 & q_1 q_2 \\ q_1 q_2 & q_2^2 \end{pmatrix} \mathbf{e}_1 \otimes \mathbf{e}_2 + \frac{\alpha_t}{|\mathbf{q}|}\begin{pmatrix} q_1^2 & -q_1 q_2 \\ -q_1 q_2 & q_2^2 \end{pmatrix} \mathbf{e}_1 \otimes \mathbf{e}_2 \tag{18}$$

**Table 1** Material parameters

| Parameter name | Variable | Value | Unit |
|---|---|---|---|
| Porosity | $\phi$ | 0.1 | [–] |
| Molecular diffusion coefficient | $d_m$ | 1.16e-9 | [$\text{m}^2$/s] |
| Longitudinal dispersion coefficient | $\alpha_l$ | 0.1 | [m] |
| Transversal dispersion coefficient | $\alpha_t$ | 0.01 | [m] |
| Concentration of injected flow | $c_{\text{in}}$ | 1 | [–] |

in which $d_m$ is the molecular diffusion coefficient. $\alpha_l$ and $\alpha_t$ are the longitudinal and transversal dispersion coefficients, respectively. $\mathbf{e}_1$ and $\mathbf{e}_2$ are the basis vectors. The quantities of these parameters are given in Table 1. The concentration-dependent viscosity $\mu^{\text{l}}(c)$ of the liquid mixture is given by, cf. [3, 5],

$$\mu^{\text{l}}(c) = \mu^{\text{a}R}\left(c + (1-c)\left[\frac{\mu^{\text{f}R}}{\mu^{\text{a}R}}\right]^{-0.25}\right)^{-4}, \tag{19}$$

in which $\mu^{\text{a}R}$ and $\mu^{\text{f}R}$ are the viscosities of the solvent fluid and the resident fluid, respectively. Moreover, the stability of the flow is characterized by the mobility factor $M$, which describes the ratio of the viscosity of the resident fluid to that of the solvent one, i.e., $M = \mu^{\text{f}R}/\mu^{\text{a}R}$. The flow tends to be instable if the mobility factor is greater than unity, when viscous fingering effects may occur. For more details concerning the evolution of viscous fingering effects, we refer to the review work [38].

### 4.1 Homogeneous domain

In the first example, we consider a homogeneous domain, see Fig. 4a. The intrinsic permeability of the porous matrix is $k^{\text{s}} = 10^{-11}\ \text{m}^{-2}$. We first compute the stable case with the mobility factor $M = 1$, which results in a constant viscosity distribution, i.e., $\mu^{\text{l}} \equiv 10^{-3}$ Pa·s. Since the computational domain is homogeneous, the pressure distribution is linear and remains constant throughout the whole process. Thus, the quantity of the filter velocity $\mathbf{q}$ can be computed analytically, i.e., $\mathbf{q} = 6.25 \times 10^{-4}$ m/s. Note that the seepage velocity $\mathbf{v}$ equals $\mathbf{v} = \mathbf{q}/\phi = 6.25 \times 10^{-3}$ m/s, which is the true propagation velocity of the solvent fluid.

As is well known, the sufficient but not necessary condition for the stability of the numerical scheme is the Courant–Friedrich–Levy condition. Given the representative element size $h$ in space and the time step size $\Delta t$, the Courant number $C_r$ can be calculated by

$$C_r = \frac{|v|\,\Delta t}{h}, \tag{20}$$

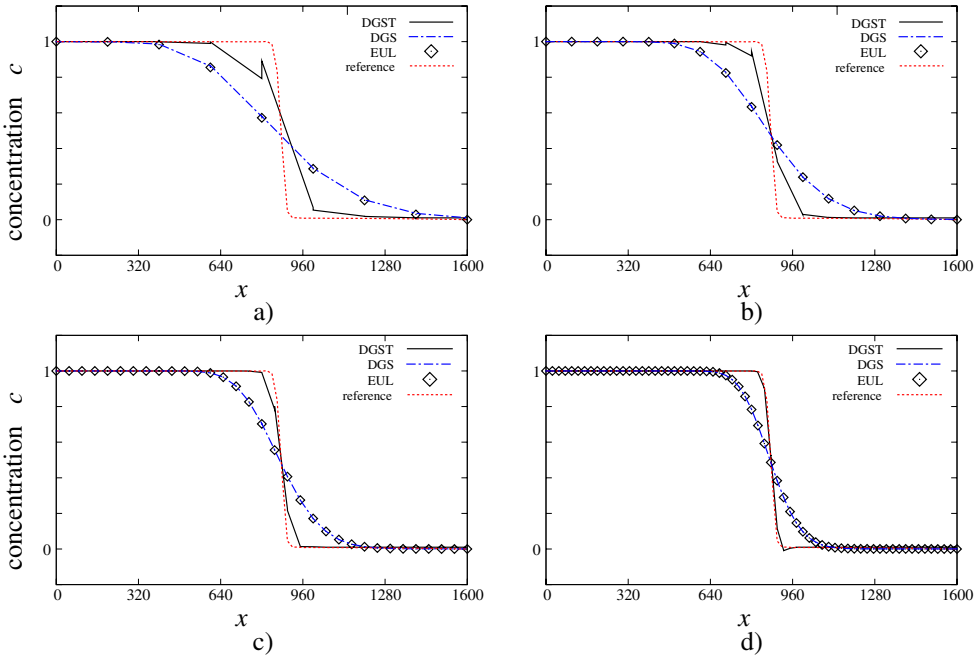


**Fig. 5** Concentration profiles at $t = 1.4 \times 10^5$ s obtained by the DGST, DGS, and EUL approaches with different spatial and temporal discretizations. (*a*) $h_0$, $\Delta t = 12{,}800$ s, (*b*) $h_1$, $\Delta t = 6{,}400$ s, (*c*) $h_2$, $\Delta t = 3{,}200$ s, (*d*) $h_3$, $\Delta t = 1{,}600$ s

where $|v|$ is the maximum wave speed within an element. Generally speaking, the Courant number has to be smaller than one, i.e., $C_r \leq 1$, to ensure numerical stability. Besides the stability criterion, the choice of an *optimal* time step size $\Delta t$ for a given finite element discretization is an important aspect in a coupled space-time finite element analysis. It is well known that the quality of the numerical solution cannot be improved extensively by simply reducing the size of time steps while holding the spatial discretization fixed [39]. In the 1-dim case, for a three-node (quadratic) element with a first-order time-stepping algorithm, the critical time step is [39]

$$\Delta t = \frac{h}{\sqrt{6}\,|v|}. \tag{21}$$

According to the problem at hand, quadratic polynomials in space and linear ones in time are chosen for the concentration $c_h$ and the pressure $p_h$. It is easy to derive that the critical time step corresponds to the Courant number $C_r \approx 0.4$.

Figure 5 shows the concentration front at $t = 1.4 \times 10^5$ s obtained by the DGST method, the spatial conforming finite element method combined with a backward Euler scheme in time (EUL), and the spatial discontinuous Galerkin method with the backward Euler scheme in time (DGS) [5]. The choice of spatial grids and the corresponding time step sizes are listed in Table 2. The sizes of the time steps are chosen according to $C_r = 0.4$.

For a qualitative comparison, a reference solution is generated by the EUL with an overkill discretization. In Fig. 5, we observe that, with respect to all four grids $h_0, \ldots, h_3$, under the same spatial and temporal discretization, the DGST method leads to the best solution in that the steep concentration front is much better resolved than the other approaches, i.e., the EUL and the DGS approaches. Moreover, inconsistent quantities, i.e., jumps, are observed in the solutions of the DGST approach obtained on relative coarse discretizations $h_0$ and $h_1$. However, it has to be mentioned, herein these jumps do not spoil the numerical results but contribute to the accuracy of the overall solutions. The quantity of the jump ($[\![ c_h ]\!]$) decreases in the numerical solutions of the finer discretizations $h_2$ and $h_3$. Note in passing that the jumps that occur in the solution of DG approaches reflect the quality of the discretizations, which

**Table 2** Choice of time step sizes $\Delta t$ of various grids $h_0, \ldots, h_3$ on homogeneous/inhomogeneous domains

| $\Delta t$ [s] | | $h_0$ | $h_1$ | $h_2$ | $h_3$ |
|---|---|---|---|---|---|
| Homogeneous domain | $M = 1$ | 12,800 | 6,400 | 3,200 | 1,600 |
| Inhomogeneous domain | $M = 1$ | – | 3,200 | 1,600 | 800 |
| Inhomogeneous domain | $M = 5$ | – | 1,600 | 800 | 400 |
| Number of elements | | $8 \times 8$ | $16 \times 16$ | $32 \times 32$ | $64 \times 64$ |

can be used as a simple but reliable error indicator for adaptive strategies, cf. [30].

In Fig. 5, we also observe that there is no significant difference between the quantity of the numerical results obtained by the EUL and the DGS method. However, the spatial DG method is well known for capturing sharp gradients that contribute to the accuracy of the overall numerical solution scheme, cf. [5, 6, 25]. According to the knowledge of the authors, so far, the spatial DG formulation is always implemented by means of semidiscrete numerical techniques, such that discontinuous approximations in space is applied to produce an ODE system, which is in turn solved by the backward Euler scheme, i.e., DGS scheme, cf. [5, 40]. However, according to our numerical experiments, we conclude that a DG approximation in space alone does not always ensure more accurate solutions, see Fig. 5. In these cases, the error introduced by the time-stepping approach, i.e., the backward Euler scheme, is dominant. Thus, an advanced spatial DG formulation cannot benefit the overall accuracy of the numerical solution. Nevertheless, we remark that, due to the employment of the discontinuous approximations in space, the number of DOFs for the solution scheme of the DGS scheme is almost four times larger than that of the spatially conforming FE method (EUL).

Next, we compute the same problem on the coarse discretization $h_0$ with the EUL and the DGS method with a much smaller time step, i.e., $\Delta t = 320$ s. For comparison, the numerical solution obtained by the DGST scheme on the same spatial mesh $h_0$ with the time step $\Delta t = 12{,}800$ s is depicted in the same figure, see Fig. 6. Herein, due to the much refined temporal discretization, slight differences in the solutions of the EUL and the DGS are observed. The concentration $c_h$ obtained by the EUL is continuous, while jumps are observed in the solution of the DGS method near the concentration front. In spite of this slight difference, no significant improvement other than that of the DGST method with a much larger time step is obtained. Further refinements in the time step size have also been tested, but they produce no significant improvements. We conclude that, in this case, the error introduced by the spatial discretization is dominant, such that a further decrease of the time step does not contribute to the quality of the solution. We denote that, in achieving those comparable solutions, the size of the time step of the DGST method is 40 times larger than those used in the DGS and the EUL approaches.

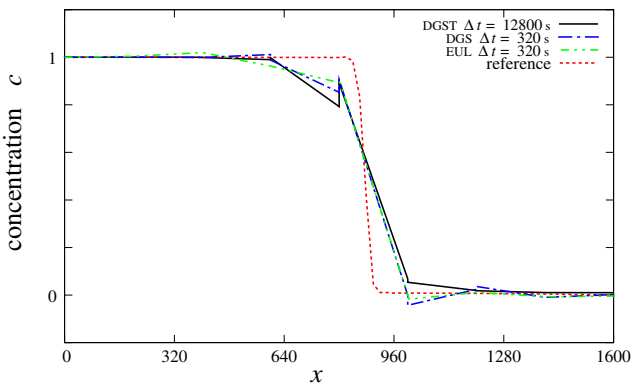


**Fig. 6** Concentration profiles at $t = 1.4 \times 10^5$ s obtained by DGST, DGS and EUL approaches with the same spatial discretization but different $\Delta t$

### 4.2 Inhomogeneous domain

Next, we consider the flow propagation in an inhomogeneous domain as depicted in Fig. 4b. The patches with dark gray color represent the less permeable material with the intrinsic permeability $k^{\mathfrak{s}} = 10^{-14}$ m$^{-2}$, which is 1,000 times smaller than those in the rest of the domain ($k^{\mathfrak{s}} = 10^{-11}$ m$^{-2}$). Since it is natural to choose a mesh whose grids are smaller than the obstacles, we perform the computations on the meshes $h_1, \ldots, h_3$.

We first consider the stable case ($M = 1$) with a constant viscosity $\mu^{\mathfrak{l}} = 10^{-3}$ Pa·s. Due to the inhomogeneity within the computational domain, the filter velocity $\mathbf{q}_h$ cannot be determined directly. However, the distribution of the fluid pressure $p_h(\mathbf{x}, t)$ is constant over time. It is easy to observe that the highest pressure

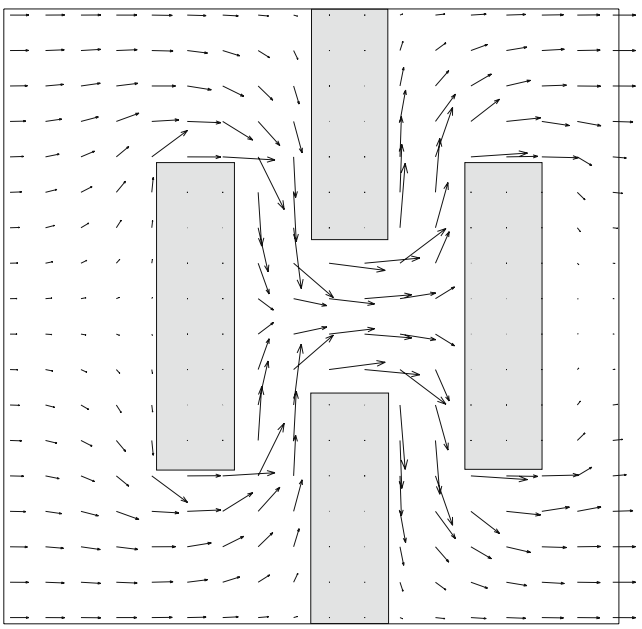

**Fig. 7** Filter velocity distribution $\tilde{\mathbf{q}}_h$ of the inhomogeneous domain with the mobility ratio $M = 1$

gradient occurs between the two parallel patches with the distance only half of the length of the complete computational domain. Hence, we can derive that the highest filter velocity $\mathbf{q}_h$ in this case is approximately twice as large as in the previous example. To ensure the stability condition, the time steps are chosen as one half of those used in the previous example, see Table 2.

Figure 7 shows the $H(\mathrm{div})$ projection of the filter velocity $\tilde{\mathbf{q}}_h$ obtained on the mesh $h_1$. We observe that there are no spurious sinks or source terms occurring in the computational domain. The necessity and quality of this $H(\mathrm{div})$ projection were discussed extensively in [34]. Moreover, as the distribution of the pressure field $p_h(\mathbf{x}, t)$ is relatively smooth, no significant improve-

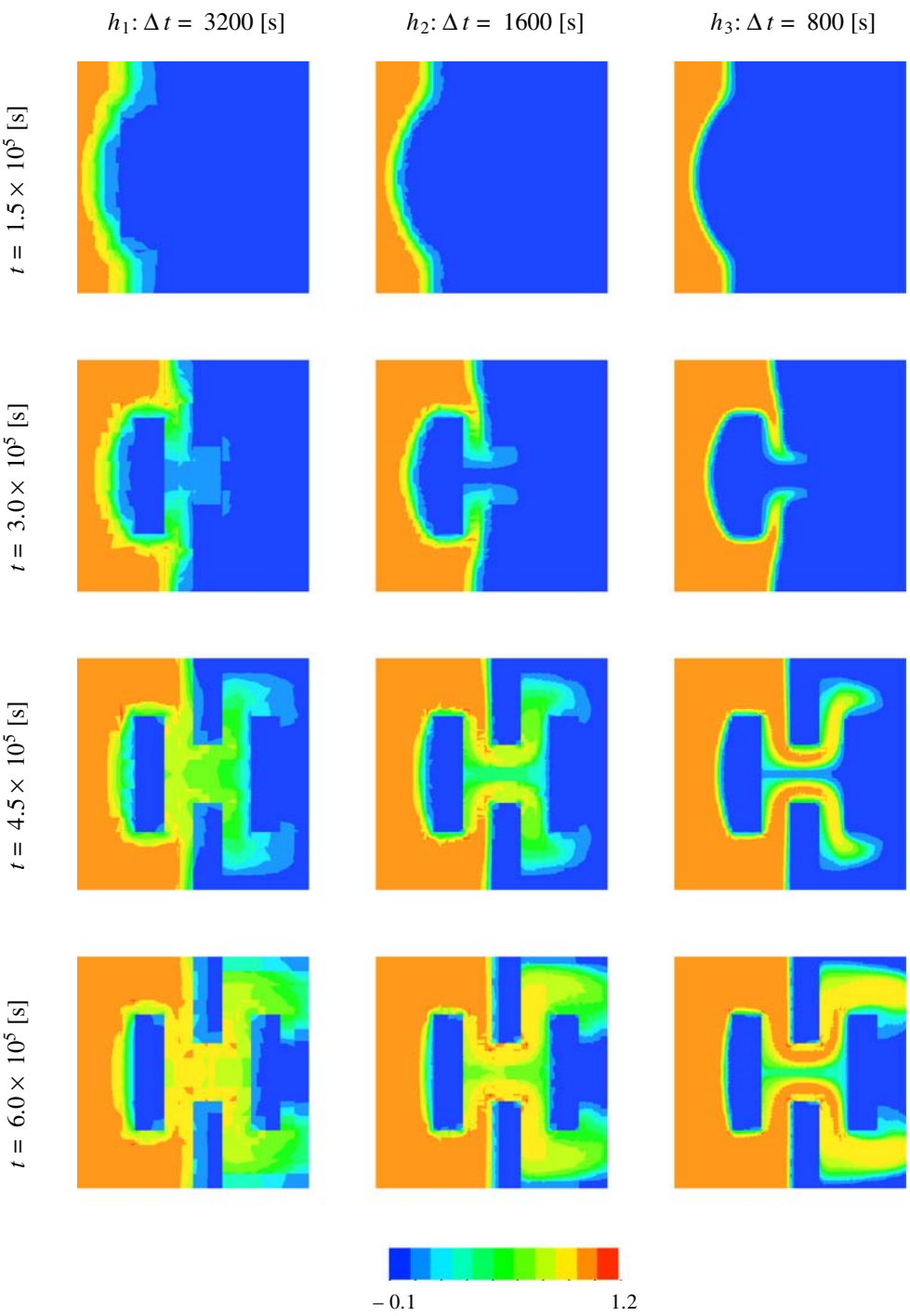


**Fig. 8** Concentration $c_h$ at various time levels $t = 1.5,\ 3.0,\ 4.5,\ 6.0 \times 10^5$ s in the inhomogeneous domain with the mobility factor $M = 1$

ments in the distribution of the filter velocities $\tilde{\mathbf{q}}_h$ are observed in the solutions of finer grids, i.e., $h_2$ and $h_3$.

Figure 8 shows the concentration profiles at different time levels, i.e., $t = 1.5,\ 3.0,\ 4.5,\ 6.0 \times 10^5$ s. Herein, we observe that the injected fluid circumvents the less permeable patches. Steep concentration fronts around these patches are well resolved, even on the coarse discretization $h_1$. The slope limiting procedure is applied to the concentration field $c^-_{h,n}$ $(n > 0)$ in a postprocessing step on each time-slab $Q^n$, i.e., $\check{c}_{h,n} = S(c^-_{h,n})$, where $S$ denotes the function of the slope-limiting procedure. Despite slight over- and undershoots around the less permeable patches, the numerical solutions are stable and reflect the propagation phenomena of the flow. It is necessary to mention that all three meshes, i.e., $h_1$, $h_2$, and $h_3$, produce qualitatively similar solutions. Of course, more accurate numerical solutions are obtained by a finer discretization. Moreover, as the mobility factor equals one, no fingering effects occur in the computational domain.

Next, we consider a physically more sophisticated case with a small mobility factor $M = 5$, i.e., $\mu^{fR} = 10^{-3}$ Pa·s and $\mu^{aR} = 2 \times 10^{-4}$ Pa·s. Thus, the viscosity $\mu^{\mathrm{f}}$ is no longer a constant but decreases with the increase of the concentration level, cf. Eq. 19. The viscosity $\mu^{\mathrm{f}}$ is computed by

$$\mu^{\mathrm{f}}(\mathbf{x}) = \begin{cases} \mu^{\mathrm{f}}(c_0(\mathbf{x})) & \text{if} \quad n = 0, \\ \mu^{\mathrm{f}}(S(c^-_{h,n}(\mathbf{x}))), & \text{otherwise.} \end{cases} \qquad \mathbf{x} \in \Omega \tag{22}$$

Since the viscosity $\mu^{\mathrm{f}}$ varies with the concentration field, the pressure distribution evolves over time. However, we denote that, due to the small mobility factor $M = 5$, the filter velocity $\mathbf{q}_h(\mathbf{x}, t)$ grows slowly as the concentration level increases. In order to account for the increase of the filter velocity, even smaller time steps are employed, see Table 2.

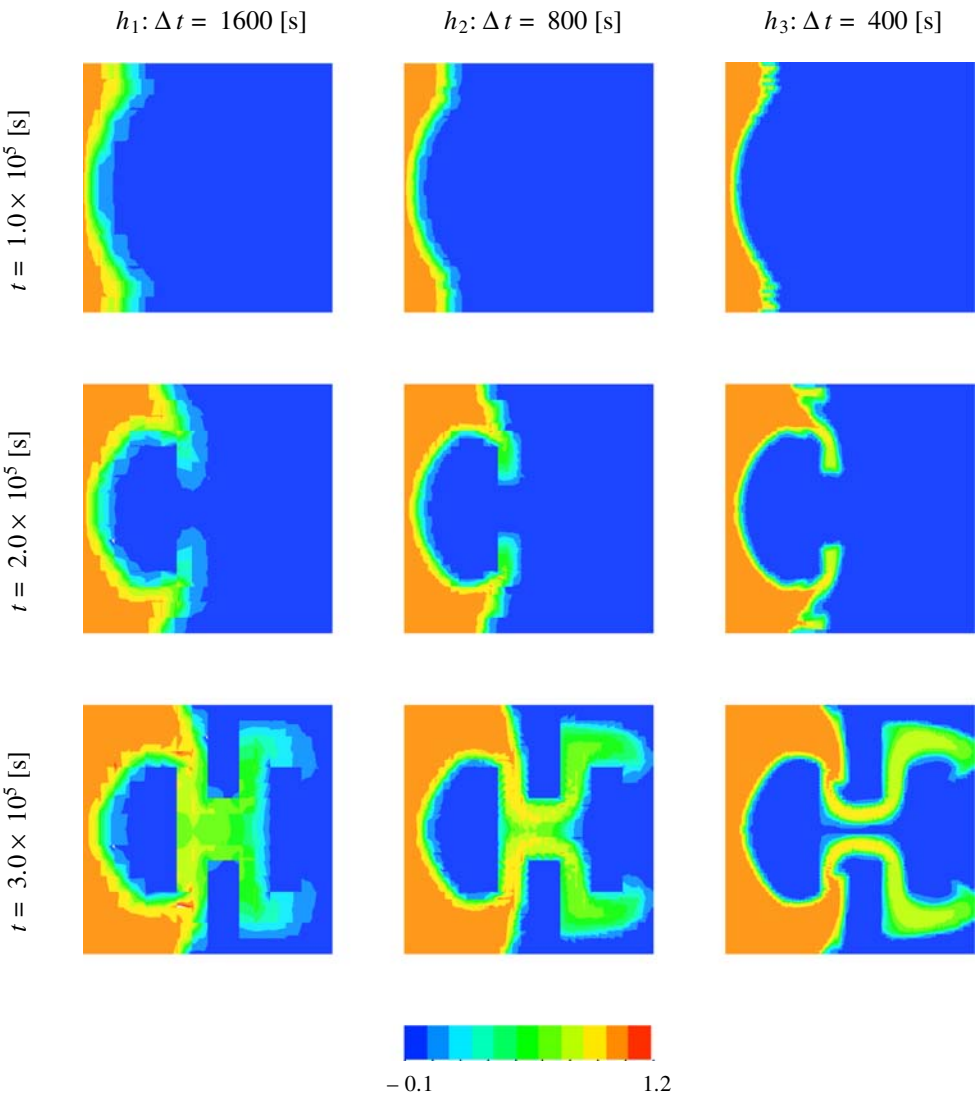


**Fig. 9** Concentration $c_h$ at various time levels $t = 1.0,\ 2.0,\ 3.0 \times 10^5$ s in the inhomogeneous domain with the mobility factor $M = 5$

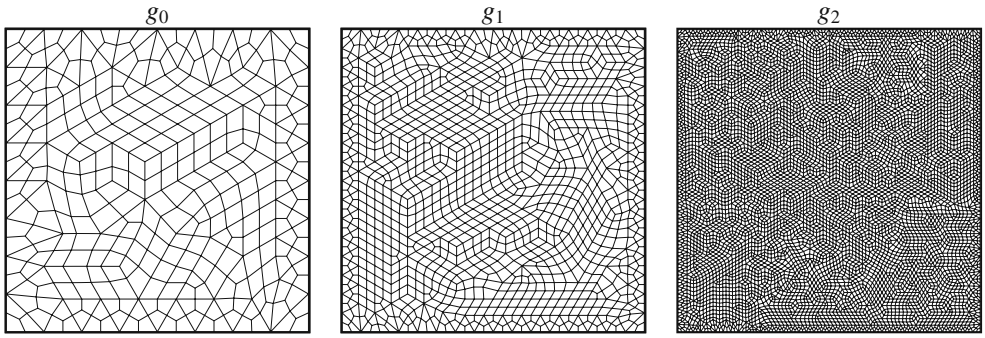


**Fig. 10** Nonconforming meshes with different mesh densities

Figure 9 shows the simulation results obtained at different time levels. Since the liquid viscosity $\mu^{\mathfrak{l}}$ decreases as the concentration level increases, the propagation of the solvent is much faster than in the previous tests, such that the solvent fluid takes almost one half of the time as in the stable case to reach the right side of the computational domain, cf. Fig. 8 and Fig. 9. Since, in the current experiment, the mobility factor is larger than one, the propagation of the flow tends to be instable. However, in the results obtained by the coarse discretizations of $h_1$ and $h_2$, such effects are not significant. In the solution of the finest discretization $h_3$, we observe that the solvent fluid tends to penetrate through the more viscous resident fluid, leaving out vacancy around the less permeable patches with very low concentration.

## 5 Heterogeneous domain

In the last example, we consider a heterogeneous domain with randomly distributed permeabilities $k^s$ in the range of $[10^{-11}$–$10^{-14}]$ m$^2$, see Fig. 4c. The boundary and initial conditions are the same as before. We compute the problem on three nonconforming grids $g_0, \ldots, g_2$ with different mesh densities, see Fig. 10. Since a direct determinant of the filter velocity is not possible, the time step sizes are chosen empirically, such that the stability of the overall solution is ensured. More details with respect to the qualities and the computational efforts of the different grids $(g_0, \ldots, g_2)$ are given in Table 3.

**Table 3** Computational effort of nonconforming meshes

| | Mesh | | |
|---|---|---|---|
| | $g_0$ | $g_1$ | $g_2$ |
| Number of elements | 332 | 1,260 | 7,704 |
| Number of DOFs/step | 10,624 | 40,320 | 246,528 |
| $\Delta t$ [s] | 200 | 100 | 50 |

We start with the computation of the stable case with the mobility factor $M = 1$, i.e., the liquid viscosity equals $\mu^{\mathfrak{l}} = 10^{-3}$ Pa·s. Here, by choosing different pairs of parameters $\sigma$ and $\epsilon$, we perform the computation with different spatial DG formulations, i.e., NIPG, SIPG, and IIPG, rf. Eqs. 16 and 17. It is well known that the choice of the penalty parameter $\sigma$ is essential for the accuracy of the solution. For the problem at hand, it is known that the penalty factor must not be "sufficiently large", rf. [14], so that we set $\sigma = 1/h$, whereas $h$ is the representative element size in space. In Fig. 11, we depicted the concentration state at $t = 1.8 \times 10^5$ s obtained by the four different spatial DG formulations. We observed, with this proper choice of the $\sigma$ factor, the penalty methods, i.e., SIPG, NIPG, and IIPG, produce very similar solutions to those of the OBB methods. In this sense, we conclude that these penalty methods are as good as the OBB formulations in modeling the propagation flow through the porous materials.

Next, we compute the same problem with a mobility factor $M = 10$, i.e., $\mu^{\mathfrak{f}R} = 10^{-3}$ Pa·s and $\mu^{\mathfrak{a}R} = 10^{-4}$ Pa·s. Figure 12 shows the concentration states obtained on meshes $g_2$ by OBB–OBB formulation at different time levels $t = 0.6,\ 1.2,\ 1.8 \times 10^5$ s. It is obvious to observe that fingers grow in the computational domain. Moreover, due to the occurrence of fingers, within the same period of time ($t = 1.8 \times 10^5$ s), the solvent fluid almost has a finger through the whole computational domain when, in the stable case, the solvent fluid has penetrated only one third of the domain, cf. Figs. 12 and 11. Moreover, there are local over- and undershoots near the steep concentration fronts. However the overall solution is stable and no degeneration of the numerical solution through local oscillations, i.e., over- and undershoots, is observed.

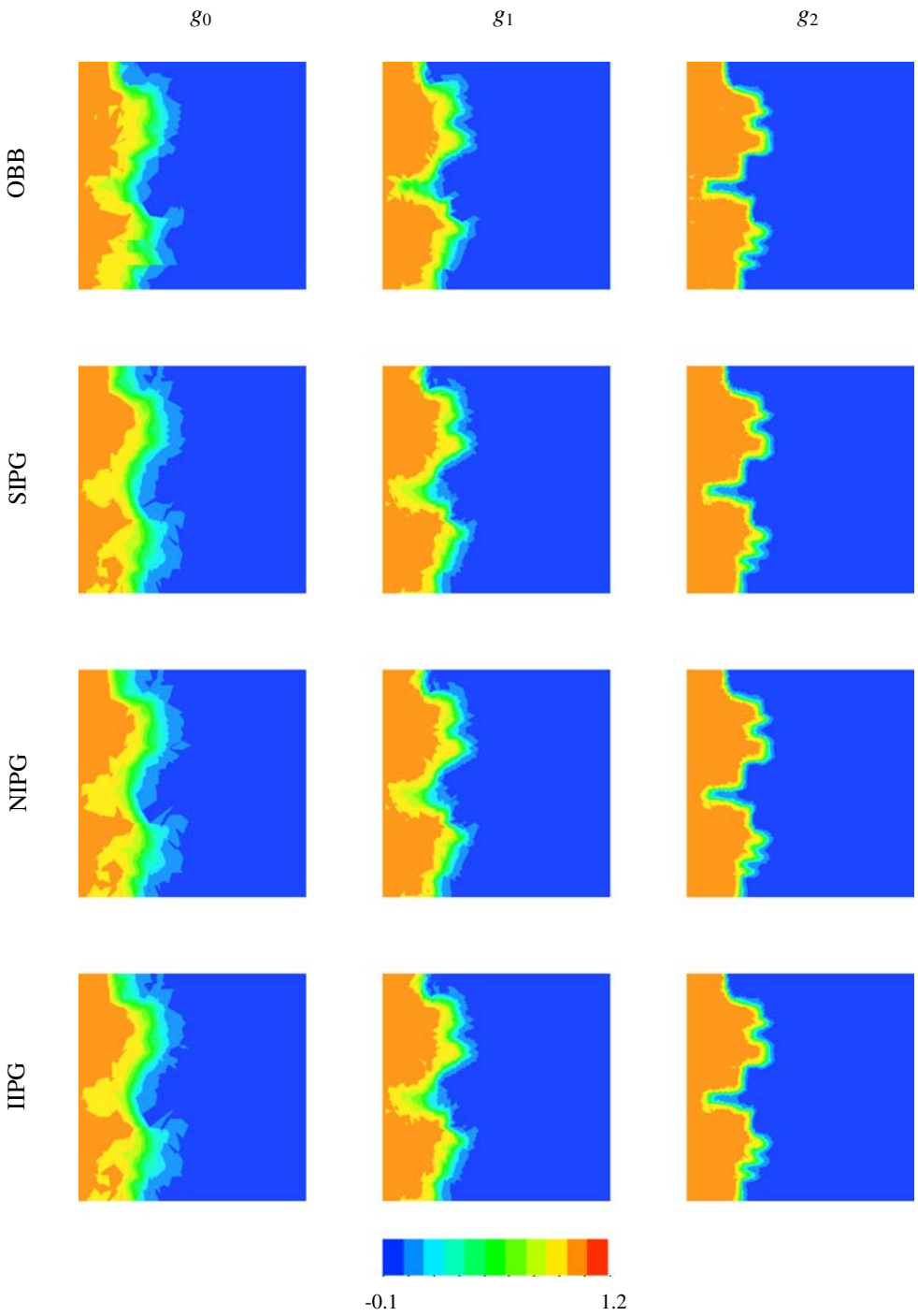


**Fig. 11** Concentration $c_h$ at $t = 1.8 \times 10^5$ s in the heterogeneous domain computed by various formulations with the mobility factor $M = 1$

## 6 Conclusions

We present an efficient coupled DGST method to model transport phenomena in porous media. Discontinuous approximations in space and in time are applied. Due to the employment of discontinuous approximations in the spatial and the temporal domains, with the same spatial and temporal discretization, the total number of DOFs of the DGST method is much larger than that of the conventional approaches. However, the extra costs of the computational effort can be well compensated by using larger discretization both

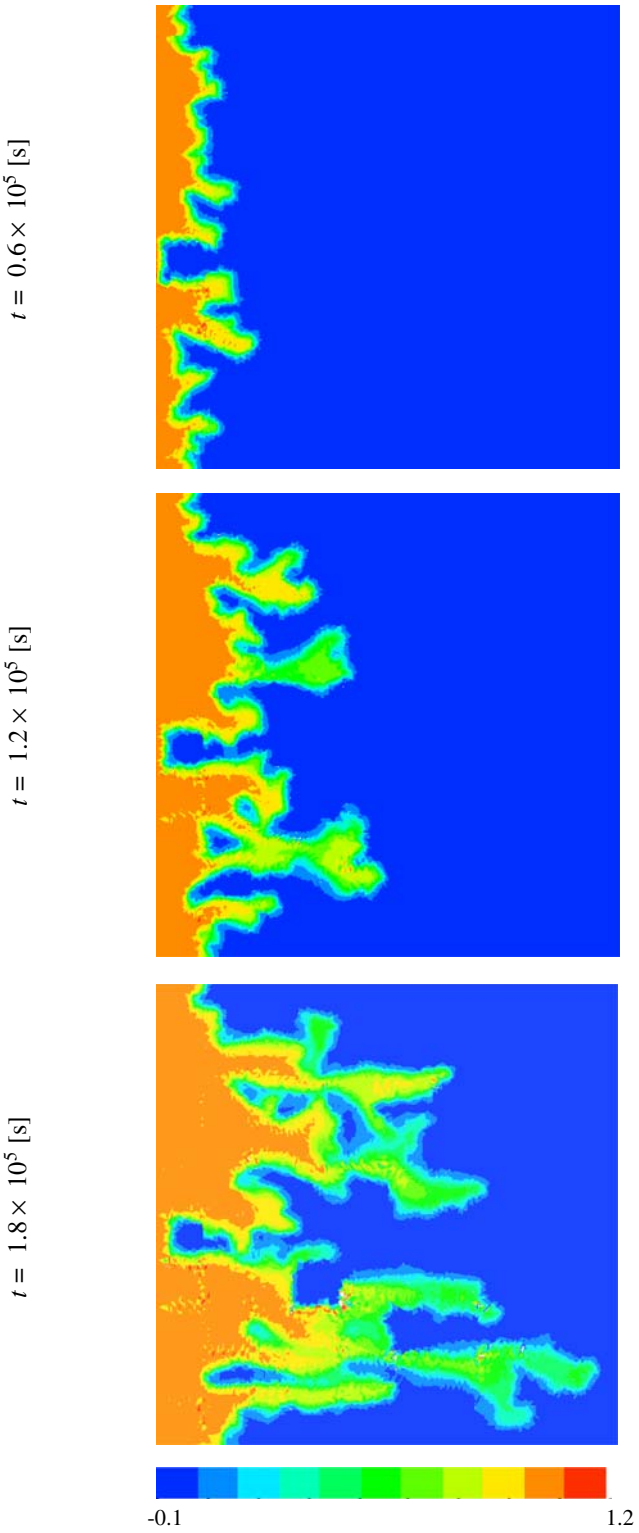


**Fig. 12** Concentration $c_h$ at various time levels $t = 0.6, 1.2, 1.8 \times 10^5$ s in the heterogeneous domain computed by OBB formulation with the mobility factor $M = 10$ on $g_2$ mesh

in space and in time. The proposed new space-time coupled formulation is able to capture steep gradients in the solution very well and is suitable for modeling more complex phenomena, i.e., viscous fingering effects. Moreover, various formulations of spatial DG methods have been tested. According to a proper choice of the penalty factor, all these approaches produce very similar solutions.

## References

1. Ewing, R.E., Wyoming, U., Russell, T.F., Wheeler, M.F.: Simulation of miscible displacement using mixed methods and a modified method of characteristics. Soc. Pet. Eng. J. 12241 (1983)
2. Douglas, J.: The numerical simulation of miscible displacement in porous media. In: Oden, J.T. (ed.) Computational Methods in Nonlinear Mechanics, pp. 225–237. North-Holland, Amsterdam (1980)
3. Koval, E.J.: A method for predicting the performance of unstable miscible displacement in heterogeneous media. Soc. Pet. Eng. J. **3**, 145–154 (1963)
4. Klieber, W., Rivière, B.: Adaptive simulations of two-phase flow by discontinuous Galerkin methods. Comput. Methods Appl. Mech. Eng. **196**, 404–419 (2006)
5. Rivière, B., Wheeler, M.F.: Discontinuous Galerkin methods for flow and transport problems in porous media. Commun. Numer. Methods Eng. **79**, 157–174 (2002)
6. Rivière, B., Wheeler, M.F., Banaś, K.: Part II: Discontinuous Galerkin methods applied to a single phase flow in porous media. Comput. Geosci. **4**, 337–349 (2000)
7. Nayagum, D., Schäfer, G., Mosé, R.: Modelling two-phase incompressible flow in porous media using mixed hybrid and discontinuous finite elements. Comput. Geotech. **8**, 49–73 (2004)
8. Oden, J.T., Babuška, I., Baumann, C.E.: A discontinuous *hp* finite element method for diffusion problems. J. Chem. Phys. **146**, 491–519 (1998)
9. Rivière, B., Wheeler, M.F., Girault, V.: Improved energy estimates for interior penalty, constrained and discontinuous Galerkin methods for elliptic problems. Part I. Comput. Geosci. **3**, 337–360 (1999)
10. Wheeler, M.F.: An elliptic collocation-finite element method with interior penalties. SIAM J. Numer. Anal. **15**, 152–161 (1978)
11. Arnold, D.N.: An interior penalty finite element method with discontinuous elements. SIAM J. Numer. Anal. **19**, 742–760 (1982)
12. Dawson, C., Proft, J.: Coupled discontinuous and continuous Galerkin finite element methods for the depth-integrated shallow water equations. Comput. Methods Appl. Mech. Eng. **193**, 289–318 (2004)
13. Sun, S., Wheeler, M.F.: Symmetric and nonsymmetric discontinuous Galerkin methods for reactive transport in porous media. SIAM J. Numer. Anal. **43**(1), 195–219 (2005)
14. Dawson, C., Sun, S., Wheeler, M.: Compatible algorithms for coupled flow and transport. Comput. Methods Appl. Mech. Eng. **193**, 2565–2680 (2004)
15. Ames, W.F.: Numerical Methods for Partial Differential Equations, 2nd edn. Academic, Boston (1977)

16. Eriksson, K., Estep, D., Hansbo, P., Johnson, C.: Computational Differential Equations. Cambridge University Press, Cambridge (1996)
17. Argyris, J.H., Scharpf, D.W.: Finite elements in space and time. Nucl. Eng. Des. **10**, 456–464 (1969)
18. Fried, I.: Finite element analysis of time-dependent phenomena. AIAA J. **7**, 1170–1173 (1969)
19. Oden, J.T.: A general theory of finite elements ii. applications. Int. J. Numer. Methods Eng. **1**, 247–259 (1969)
20. Hughes, T.J.R., Hulbert, G.M.: Space-time finite element methods for elastodynamics: Formulations and error estimates. Comput. Methods Appl. Mech. Eng. **66**, 339–363 (1988)
21. Hulbert, G.: Space-time finite element methods for second order hyperbolic equations. PhD thesis, Department of Mechanical Engineering, Stanford University, Stanford (1989)
22. Hulbert, G.M.: Time finite element methods for structural dynamics. Int. J. Numer. Methods Eng. **33**, 307–331 (1992)
23. Hulbert, G.M., Hughes, T.J.R.: Space-time finite element methods for second-order hyperbolic equations. Comput. Methods Appl. Mech. Eng. **84**, 327–348 (1990)
24. Chen, Z., Steeb, H., Diebels, S.: A time-discontinuous Galerkin method for the dynamical analysis of porous media. Int. J. Numer. Anal. Methods Geomech. **30**, 1113–1134 (2006)
25. Baumann, C.E.: An *hp*-adaptive discontinuous finite element method for computational fluid dynamics. PhD thesis, The University of Texas at Austin (1997)
26. Hassanizadeh, S.M., Gray, W.G.: High velocity flow in porous media. Transp. Porous Med. **2**, 521–531 (1987)
27. Diebels, S., Ehlers, W., Markert, B.: Neglect of the fluid-extra stresses in volumetrically coupled solid-fluid problems. Z. Angew. Math. Mech. **81**, S521–S522 (2001)
28. Ehlers, W.: Foundations of multiphasic and porous materials. In: Ehlers, W., Bluhm, J. (eds.) Porous Media: Theory, Experiments and Numerical Applications, pp. 3–86. Springer, Berlin (2002)
29. Baumann, C.E., Oden, J.T.: A discontinuous *hp* finite element method for convection-diffusion problems. Comput Methods Appl. Mech. Eng. **175**, 311–341 (1999)
30. Cockburn, B.: Discontinuous Galerkin methods. Z. Angew. Math. Mech. **11**, 731–754 (2003)
31. Oden, J.T., Babuška, I., Baumann, C.E.: A discontinuous *hp* finite element method for diffusion problems. J. Comput. Phys. **146**, 491–519 (1998)
32. Marsden, J.E., Hughes, T.J.R.: Mathematical Foundations of Elasticity. Dover, New York (1983)
33. Wriggers, P.: Konsistente Linearisierung in der Kontinuumsmechanik und ihre Anwendung auf die Finite-Element-Methode, Bericht Nr. F88/4 (1999) Institut für Baustatik und Numerische Mechanik, Univerität Honnover (1988)
34. Bastian, P., Rivière, B.: Superconvergence and $h(div)$-projectin for discontinuous Galerkin methods. Int. J. Numer. Methods Fluids **42**, 1043–1057 (2003)
35. Cockburn, B., Shu, C.W.: The Runge-Kutta discontinuous Galerkin method for conservation laws V. J. Chem. Phys. **141**, 199–224 (1998)
36. Hoteit, H., Ackerer, P., Mosé, R., Erhel, J., Philippe, B.: New two-dimensional slope limiters for discontinuous galerkin methods on arbitrary meshes. Int. J. Numer. Methods Eng. **61**, 2566–2593 (2004)
37. Ewing, R.E. (ed.): The Mathematics of Reservoir Simulation. SIAM, Philadelphia (1983)
38. Homsy, G.M.: Viscous fingering in porous media. Ann. Rev. Fluid Mech. **19**, 271–311 (1987)
39. Hughes, T.J.R.: The Finite Element Method. Prentice-Hall, Englewood Cliffs (1987)
40. Baumann, C.E., Oden, J.T.: An adaptive-order discontinuous Galerkin method for the solution of the Euler equations of gas dynamics. Int. J. Numer. Methods Eng. **47**(1–3), 61–73 (2000)